

Article

The Effect of Hot Oscillatory Pressing Temperature on Microstructure and Tensile Behavior of Powder Metallurgy Superalloy

Guizhong Li ^{1,2} , Dejian Sun ^{1,2,*}, Jiachen Kang ^{1,2}, Yang Gao ^{1,2}, Xuwei Yan ³ , Qiancheng Gao ^{1,2} and Ka Gao ^{4,*}

¹ School of Materials Science and Engineering, Zhengzhou University of Aeronautics, Zhengzhou 450046, China

² Henan Provincial Key Laboratory of Aeronautical Materials and Application Technology, Zhengzhou University of Aeronautics, Zhengzhou 450046, China

³ School of Aero Engine, Zhengzhou University of Aeronautics, Zhengzhou 450046, China

⁴ School of Mechanical Engineering, University of Shanghai for Science and Technology, Shanghai 200093, China

* Correspondence: sjedu@zua.edu.cn (D.S.); gaoka922@163.com (K.G.)

Abstract: The effect of the hot oscillatory pressing (HOPing) temperature on the microstructure and tensile behavior of the powder metallurgy superalloys was investigated and compared with those of the hot pressed (HPed) sample. The results show that as the HOPing temperature rises, the pores and residual dendrites disappear, the grain size becomes coarser and more uniform, the prior particle boundaries (PPBs) scale decreases; the yield strength decreases gradually; the ultimate tensile strength and elongation increase first and then decrease; the tensile property stability gradually increases. The highest ultimate tensile strength and elongation of 1403 MPa and 35%, respectively, are reached when the HOPing temperature is 1160 °C. The fracture mode of the sample hot oscillatory pressed (HOPed) at 1160 °C is a transgranular and intergranular mixed fracture. Compared with the HPed sample, room temperature tensile properties of the HOPed sample improve remarkably due to the reduced size and density of PPBs precipitates.

Keywords: powder metallurgy superalloys; hot oscillatory pressing; tensile behavior; prior particle boundary



Citation: Li, G.; Sun, D.; Kang, J.; Gao, Y.; Yan, X.; Gao, Q.; Gao, K. The Effect of Hot Oscillatory Pressing Temperature on Microstructure and Tensile Behavior of Powder Metallurgy Superalloy. *Metals* **2022**, *12*, 1652. <https://doi.org/10.3390/met12101652>

Academic Editor: Alberto Campagnolo

Received: 29 August 2022

Accepted: 27 September 2022

Published: 30 September 2022

Publisher's Note: MDPI stays neutral with regard to jurisdictional claims in published maps and institutional affiliations.



Copyright: © 2022 by the authors. Licensee MDPI, Basel, Switzerland. This article is an open access article distributed under the terms and conditions of the Creative Commons Attribution (CC BY) license (<https://creativecommons.org/licenses/by/4.0/>).

1. Introduction

Superalloys have been widely used in aero-engine hot-end parts, such as turbine discs, because of their excellent microstructural uniformity and high-temperature mechanical properties [1–5]. The materials prepared by the traditional cast-wrought process are prone to macroscale segregation, which greatly damages the ductility and hot-work properties of the superalloy [6–9].

The powder metallurgy (PM) process can effectively inhibit the formation of segregation [10–12]. Hot isostatic pressing (HIPing) technology is usually used to fabricate powder metallurgy superalloys, but the Hot isostatic pressed (HIPed) superalloys contain a large number of prior particle boundaries (PPBs) and ununiform grains, leading to poor tensile properties [13–19]. The PPBs and coarse grains are commonly eliminated by hot working, such as hot extrusion and isothermal forging [20–24], but the preparation cost increases significantly. So, it is critical to improve the performance of the as-sintered materials at a low cost.

Recently, a new powder consolidation technology, hot oscillatory pressing (HOP), has been developed, which provides pressure with controlled frequency and amplitude [25]. The technique is widely used to prepare many materials, including ceramics, metals, and composites; the results show that HOP can significantly promote densification and

inhibit grain growth [26–30]. Our previous studies [31] have also shown that HOP could effectively inhibit the formation of PPBs and significantly improve the tensile properties of the materials. However, the effect of HOPing temperature on microstructure and tensile fracture behavior has not been explored yet.

FGH4096 is one of the second-generation PM superalloys. Compared with the first-generation PM superalloys, it has higher damage tolerance and crack propagation resistance, so it is significant to study the tensile fracture behavior. In this paper, the FGH4096 was prepared by HOPing at five representative temperatures and compared with the hot pressed (HPed) sample to investigate the influence of oscillating pressure and HOPing temperature on the microstructures and tensile behaviors of the samples.

2. Materials and Methods

The chemistry of the starting alloy (FGH4096) is 16.00Cr, 12.70Co, 3.64Ti, 2.02Al, 0.68Nb, 3.91Mo, 0.02B, and Ni balance (wt%). The powders were sieved to pass 53 μm , then placed into a high-purity graphite die and HOPed with a pressure of 70 ± 10 MPa/5 Hz at 1040 $^{\circ}\text{C}$, 1080 $^{\circ}\text{C}$, 1120 $^{\circ}\text{C}$, 1160 $^{\circ}\text{C}$, and 1200 $^{\circ}\text{C}$ (details of the processing can be found in [31]). The HPed sample was prepared at 1200 $^{\circ}\text{C}$ because stable tensile properties were obtained at this temperature, and the HPing pressure was always 80 MPa. To simplify the description, the samples HOPed at 1040 $^{\circ}\text{C}$, 1080 $^{\circ}\text{C}$, 1120 $^{\circ}\text{C}$, 1160 $^{\circ}\text{C}$, and 1200 $^{\circ}\text{C}$ were named as 1040 $^{\circ}\text{C}$ -HOP, 1080 $^{\circ}\text{C}$ -HOP, 1120 $^{\circ}\text{C}$ -HOP, 1160 $^{\circ}\text{C}$ -HOP, and 1200 $^{\circ}\text{C}$ -HOP, respectively. And the sample HPed at 1200 $^{\circ}\text{C}$ was named 1200 $^{\circ}\text{C}$ -HP. Figure 1 shows the sintering process of the sample prepared by HPing and HOPing at 1200 $^{\circ}\text{C}$ as an example. The sintering process of other HOPed samples is the same as that of the 1200 $^{\circ}\text{C}$ -HOP, except for temperature.

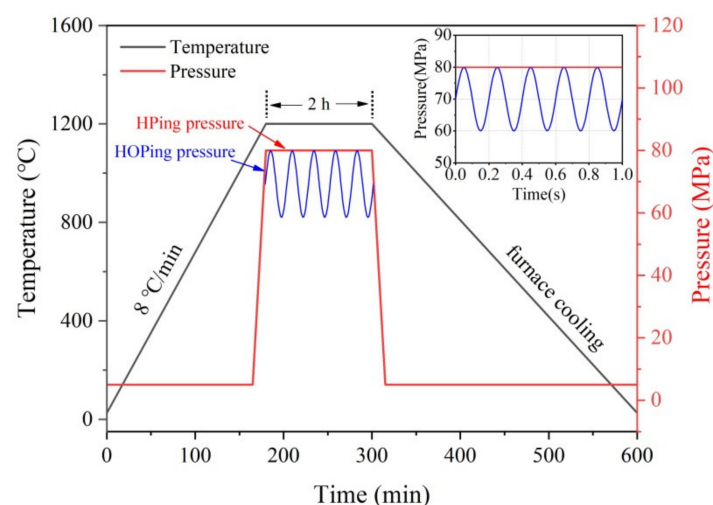


Figure 1. The sintering process of the HOPing and HPing samples at 1200 $^{\circ}\text{C}$.

The resultant samples were characterized by optical microscope (OM), scanning electron microscope (SEM), X-ray diffraction (XRD), and electron backscattering diffraction (EBSD). After the standard metallographic process, the samples were electrolytically polished (20% H_2SO_4 + 80% CH_3OH , 30 V, 15 S). The grain structure of the samples etched in 18 g CuSO_4 + 100 mL HCl + 50 mL H_2O for 25–30 s was observed by OM and EBSD. Phase identification was carried out using XRD and the precipitate distribution was observed by SEM. To better study the PPBs, the samples were etched in 3% H_2SO_4 + 5% HNO_3 + 92% HCl for 2–5 s and observed using OM. The γ matrix was removed by electrolytic etching in the solution of 10% H_3PO_4 + 90% H_2O at 5 V for 2–5 s to observe the morphology of γ' phases.

The tensile specimen is plate-shaped, and the dimension of gage section is 12.5 mm \times 3.2 mm \times 2.1 mm. Tensile testing was performed with a displacement rate of 1.5 mm/min

without the use of an extensometer. The morphology features of the tensile fractured samples were observed using SEM and OM.

3. Results

3.1. Microstructure Evolution

Figure 2 presents the grain structure of the samples with various processes. Only a few pores are observed in the 1040 °C-HOP sample (Figure 2a), and when the HOPing temperature is increased to 1080 °C, the samples are fully dense. The residual dendrites are observed in the samples HOPed at and below 1080 °C. Moreover, part of PPBs is wrapped in twins observed in the samples HOPed at 1120 °C, 1160 °C, and 1200 °C (as shown in the blue wireframe in Figure 2c,e). The grain structure of the 1200 °C-HP sample is similar to that of the 1200 °C-HOP sample (Figure 2e,f).

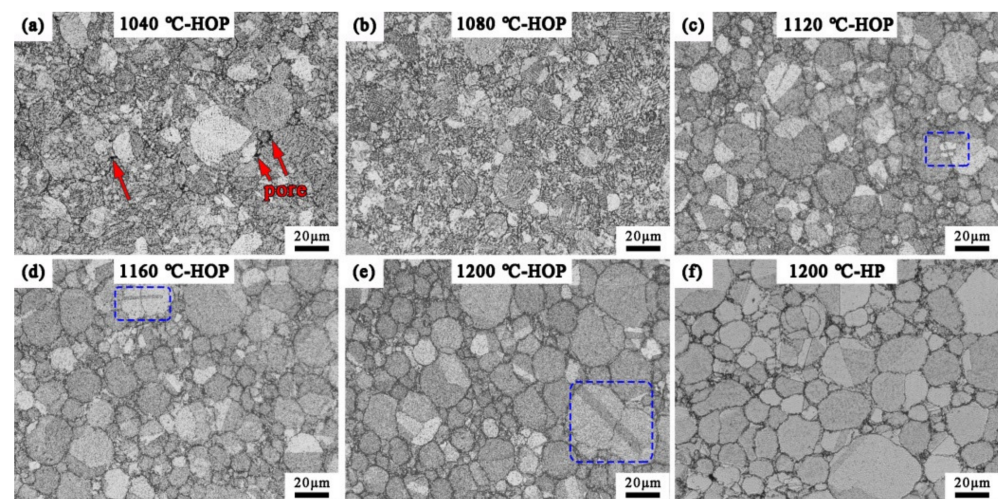


Figure 2. The grain structure of the HOPed and HPed samples: (a) 1040 °C-HOP; (b) 1080 °C-HOP; (c) 1120 °C-HOP; (d) 1160 °C-HOP; (e) 1200 °C-HOP; (f) 1200 °C-HP.

PPBs are also one of the microstructure characteristics in the PM superalloys, as they could lead to poor ductility and inter-particle fracture. The detailed characterization of the PPBs is given in Figure 3. The powder particle profile of samples HOPed at 1040–1080 °C was outlined by the ordered dendrite structure inside the particles, while the PPBs were observed in samples HOPed at 1120–1200 °C. Ingesten N. et al. proposed a method for evaluating the PPBs scale [32], which is based on the continuity of PPBs precipitates. According to this method, the PPBs scales of the samples HOPed at 1120 °C, 1160 °C, and 1200 °C are 3, 2, and 1, respectively, and that of the 1200 °C-HP sample is 2. Compared with the 1200 °C-HOP sample, more black precipitates were observed in the 1200 °C-HP sample. So, XRD analysis (as shown in Figure 4) shows that the peak of the TiC phase is found in the as-sintered materials, whereas it is not observed in the as-received powders; with the increasing HOPing temperature, the XRD peak intensity of the TiC phase increases. Compared with the 1200 °C-HOP sample, the peak intensity of the TiC phase in the 1200 °C-HP sample is higher. In addition, there are a few more peaks with low intensity in the 1160 °C-HOP, which are indexed by jade to be possibly HfO₂. But due to its low content with little impact on the performance, it will not be studied in this work.

Phase identification was carried out using EDS. And the results are shown in Figure 5. It can be seen that the white phases (shown as “1” in Figure 5a) are Mo- and Cr-enriched borides, the dark gray phases (shown as “2” in Figure 5a) are γ' phases, the black phases (shown as “3” in Figure 5a) are TiC phases, and the light gray phases (shown as “4” in Figure 5a) are γ phases.

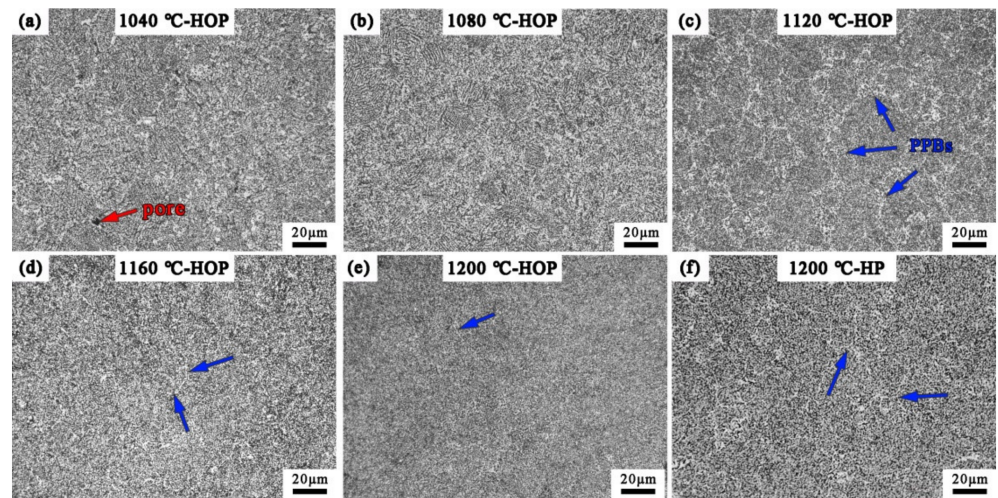


Figure 3. PPBs of the HOPed and HPed samples: (a) 1040 °C-HOP; (b) 1080 °C-HOP; (c) 1120 °C-HOP; (d) 1160 °C-HOP; (e) 1200 °C-HOP; (f) 1200 °C-HP.

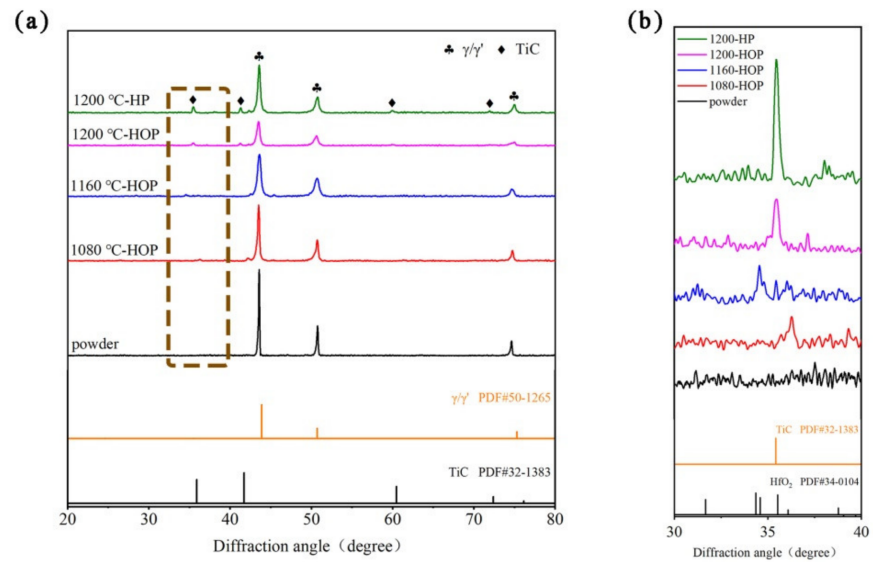


Figure 4. X-ray diffraction (XRD) analysis of the samples with various processes: (a) overall profile; (b) the enlarged profile of the dashed box in Figure 4a.

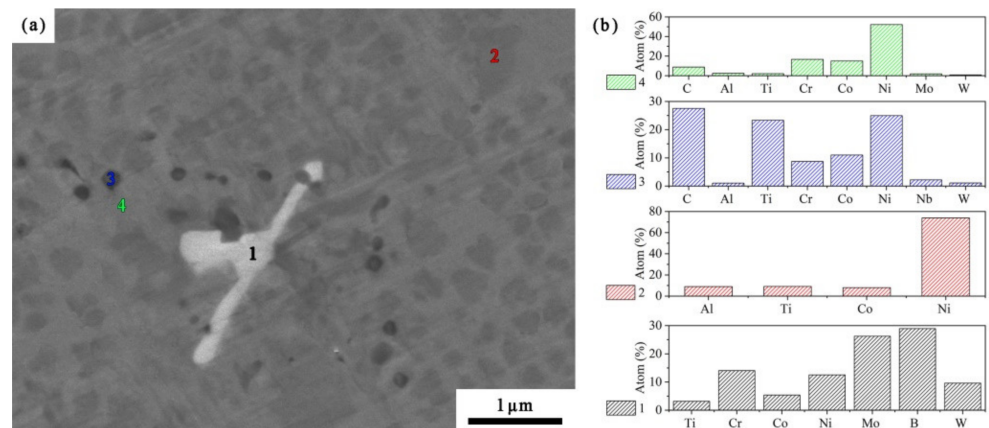


Figure 5. (a) BSE image of the 1200 °C-HP sample; (b) EDS analysis.

The precipitate distribution was examined, as shown in Figure 6. The PPBs precipitates of the samples consist of primary γ' phases, carbides, and partial borides. With the increasing HOPing temperature, the number of borides within particles decreases, while the size and density of borides on PPBs increase. Table 1 lists some precipitate sizes and volume fractions of HOPed and HPed samples. It can be found that with the increasing HOPing temperature, the size of all precipitates increases, and the volume fraction of carbides and borides also increases, except for the volume fraction of borides in the 1200 °C-HOP sample. The volume fraction of the primary γ' phase rises when the HOPing temperature increases to 1080 °C, and then it decreases slightly. Compared with the 1200 °C-HOP sample, the 1200 °C-HP sample contains more carbides and borides of a large size.

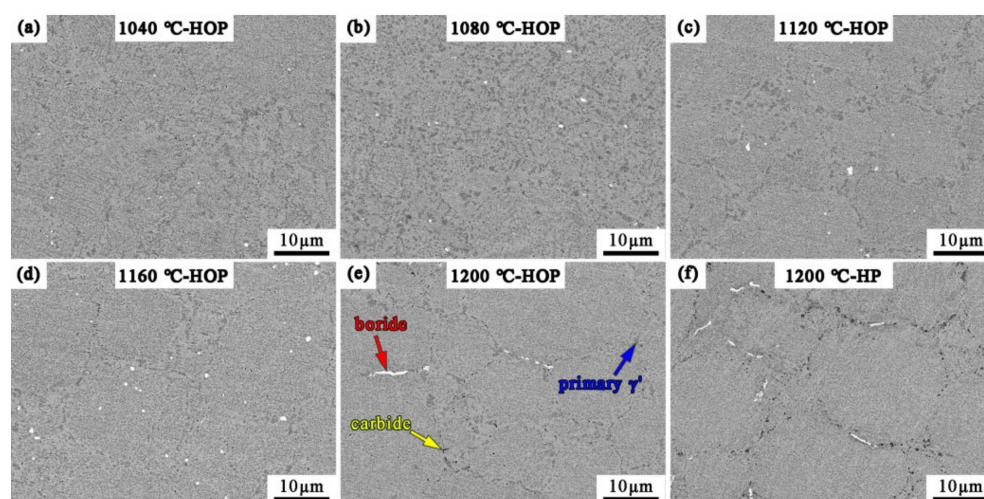


Figure 6. BSE images of the HOPed and HPed samples: (a) 1040 °C-HOP; (b) 1080 °C-HOP; (c) 1120 °C-HOP; (d) 1160 °C-HOP; (e) 1200 °C-HOP; (f) 1200 °C-HP.

Table 1. The precipitate size and volume fraction of the HOPed and HPed samples.

	Carbide		Boride		Primary γ'	
	Size/ μm	Volume Fraction/%	Size/ μm	Volume Fraction/%	Size/ μm	Volume Fraction/%
1040 °C-HOP	0.21	0.21	0.48	0.12	1.32	1.77
1080 °C-HOP	0.23	0.25	0.60	0.16	1.51	2.14
1120 °C-HOP	0.24	0.32	0.64	0.17	1.52	2.07
1160 °C HOP	0.33	0.39	0.63	0.24	1.65	1.98
1200 °C HOP	0.53	0.56	1.19	0.18	2.02	1.96
1200 °C-HP	0.67	0.67	1.68	0.28	1.94	1.92

The size and morphology of γ' phases were analyzed by removing the γ matrix using electrolytic etching, as shown in Figure 7. The results show that all the samples contain the following three types of γ' phases:

1. Primary γ' phases (shown by the blue arrow in Figure 7) are located on PPBs with a size of about 2 μm . With the increasing HOPing temperature, their morphology changes from bulk to chain-like;
2. Secondary γ' phases (shown by the green arrow in Figure 7) are located within the particles, with a size of about 500 nm. Their morphologies change from spherical to cubic or butterfly-like with the increase in HOPing temperature;
3. Tertiary γ' phases (shown by the yellow arrow in Figure 7) are located between primary γ' phases and secondary γ' phases and are less than 100 nm.

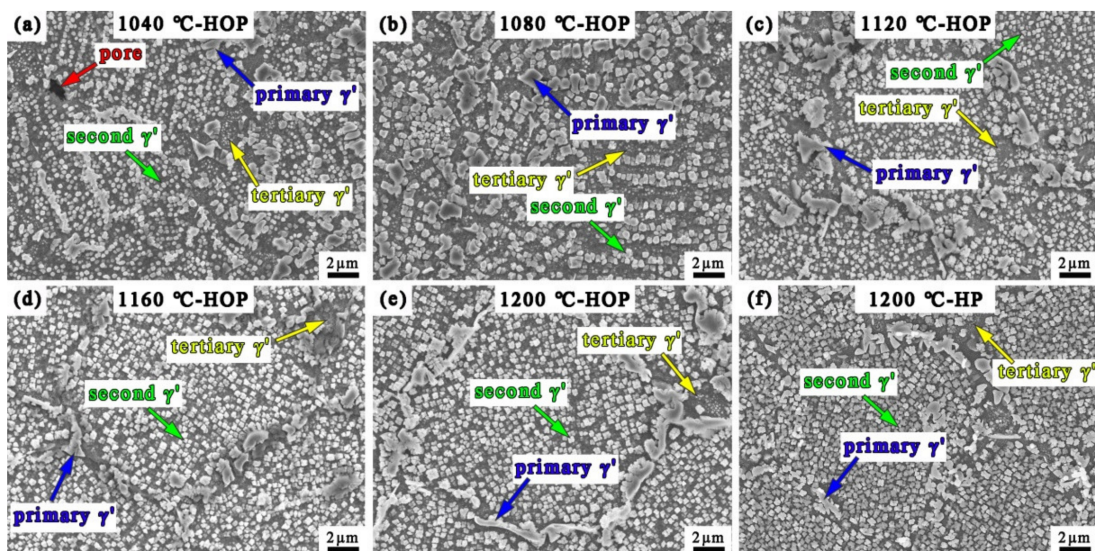


Figure 7. The morphology of the γ' phases of the HOPed and HPed samples: (a) 1040 °C-HOP; (b) 1080 °C-HOP; (c) 1120 °C-HOP; (d) 1160 °C-HOP; (e) 1200 °C-HOP; (f) 1200 °C-HP.

3.2. Tensile Properties and Fracture Behavior

Figure 8 presents the room temperature tensile properties of the HOPed and HPed samples. With the increasing HOPing temperature, the yield strength decreases, the ultimate tensile strength of the samples HOPed at 1040–1160 °C remains about 1400 MPa and then decreases significantly, and the elongation of the samples HOPed at 1040–1160 °C increases and then decreases. In conclusion, the best room temperature tensile properties are reached when the HOPing temperature is reached at 1160 °C. Moreover, with the increasing HOPing temperature, the stability of tensile properties is improved. Compared with the 1200 °C-HOP sample, the 1200 °C-HP sample has lower tensile strength and elongation.

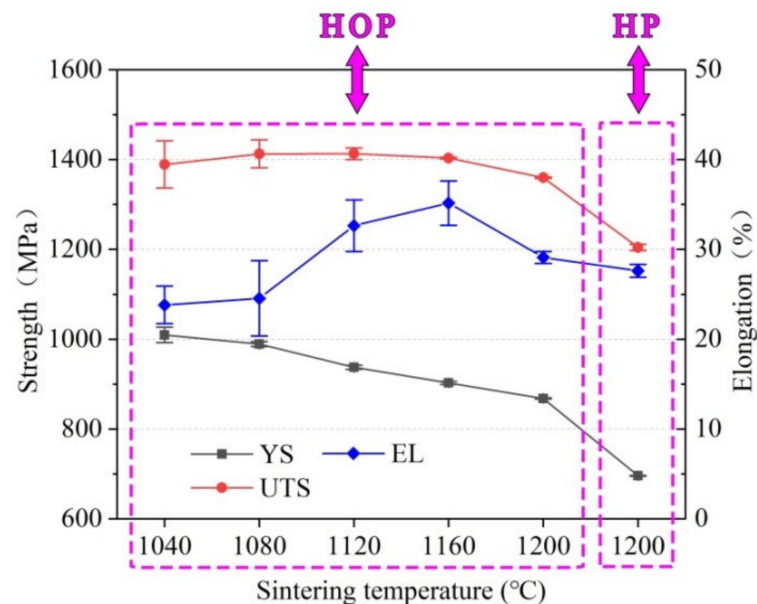


Figure 8. Room temperature tensile properties of the HOPed and HPed samples.

The fracture surfaces of the HOPed and HPed samples are shown in Figure 9. Due to particle debonding, the 1040 °C-HOP and 1080 °C-HOP samples present inter-particle fracture (red arrow in Figure 9). The intergranular fracture is observed when the HOPing temperature increases to 1120 °C (blue arrow in Figure 9), and the transgranular fracture is

observed when the HOPing temperature increases to 1160 °C (yellow arrow in Figure 9). Compared with the 1200 °C-HOP sample, the 1200 °C-HP sample presents an obvious inter-particle fracture (Figure 9f).

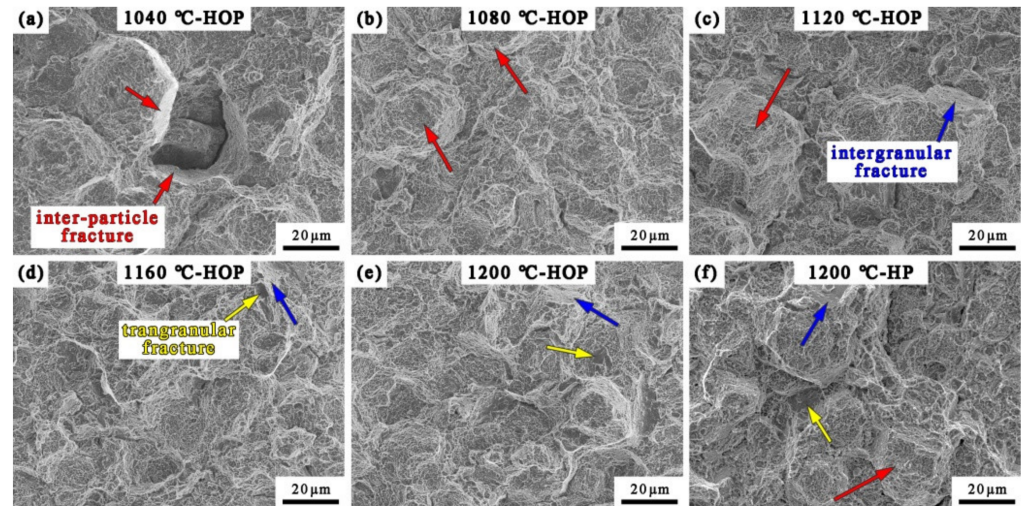


Figure 9. Fracture surfaces of the HOPed and HPed samples: (a) 1040 °C-HOP; (b) 1080 °C-HOP; (c) 1120 °C-HOP; (d) 1160 °C-HOP; (e) 1200 °C-HOP; (f) 1200 °C-HP.

Figure 10 shows the longitudinal fracture surface of the HOPed and HPed samples. The cracks of the samples HOPed at 1040–1080 °C mainly propagate along the particle boundaries (red arrow in Figure 10). When the HOPing temperature increases to 1120 °C, intergranular cracks (blue arrow in Figure 10) are observed. And the transgranular cracks (yellow arrow in Figure 10) are observed when the HOPing temperature is above 1160 °C. In comparison with the 1200 °C-HOP sample, more intergranular cracks are presented in the 1200 °C-HP sample.

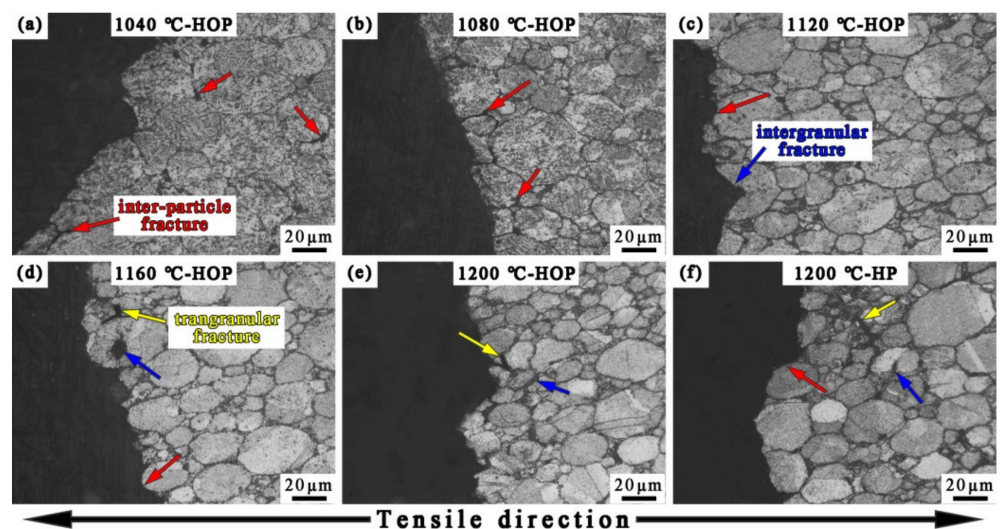


Figure 10. Microstructure nearby the longitudinal fracture surfaces of the HOPed and HPed samples: (a) 1040 °C-HOP; (b) 1080 °C-HOP; (c) 1120 °C-HOP; (d) 1160 °C-HOP; (e) 1200 °C-HOP; (f) 1200 °C-HP.

The mechanism of crack initiation was investigated using SEM, as shown in Figure 11. It could be seen that pores are the main crack origins of the 1040 °C-HOP sample. For dense samples, the crack initiation occurs near the coarse primary γ' phases in the samples HOPed at 1080–1120 °C, while the crack initiation of samples HOPed at 1160–1200 °C is

mostly on borides. Although in the 1200 °C-HP sample, the cracks also initiate on PPBs borides, microcracks are denser than in the 1200 °C-HOP sample. Interestingly, cracks are usually initiated at large borides rather than the small ones.

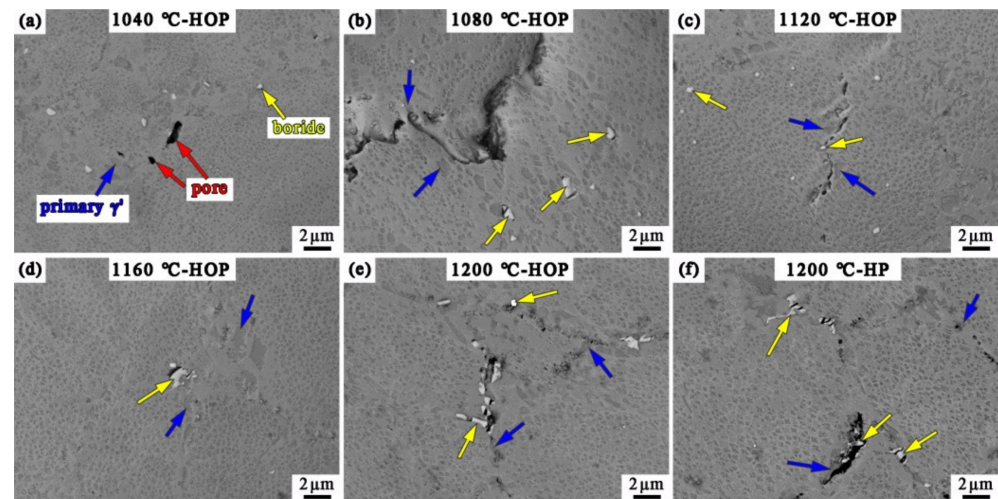


Figure 11. BSE images near the fracture surface of the HOPed and HPed samples: (a) 1040 °C-HOP; (b) 1080 °C-HOP; (c) 1120 °C-HOP; (d) 1160 °C-HOP; (e) 1200 °C-HOP; (f) 1200 °C-HP.

4. Discussion

4.1. Microstructure Evolution of the HOP Samples

Figure 12 presents the orientation images and the grain size distribution of the samples HOPed at 1080–1200 °C. The average grain size of these samples is listed in Table 2. With the increasing HOPing temperature, the grain size will increase. The most obvious increase is between 1120 and 1160 °C, and the number and area of small grains (less than 10 μm) decrease significantly (as shown in Figure 12e,f). In addition, with the increasing HOPing temperature, the grain size uniformity also increases, as shown in Figure 12f. The distribution of grain size changes from the approximate monotonic distribution (1080–1120 °C) to the normal distribution (1160–1200 °C).

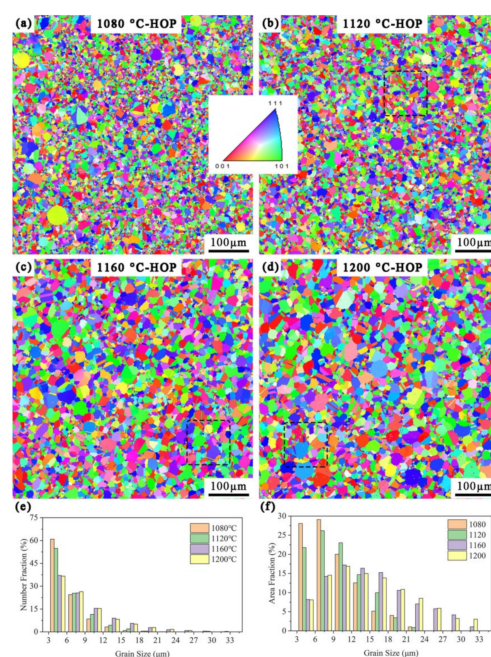
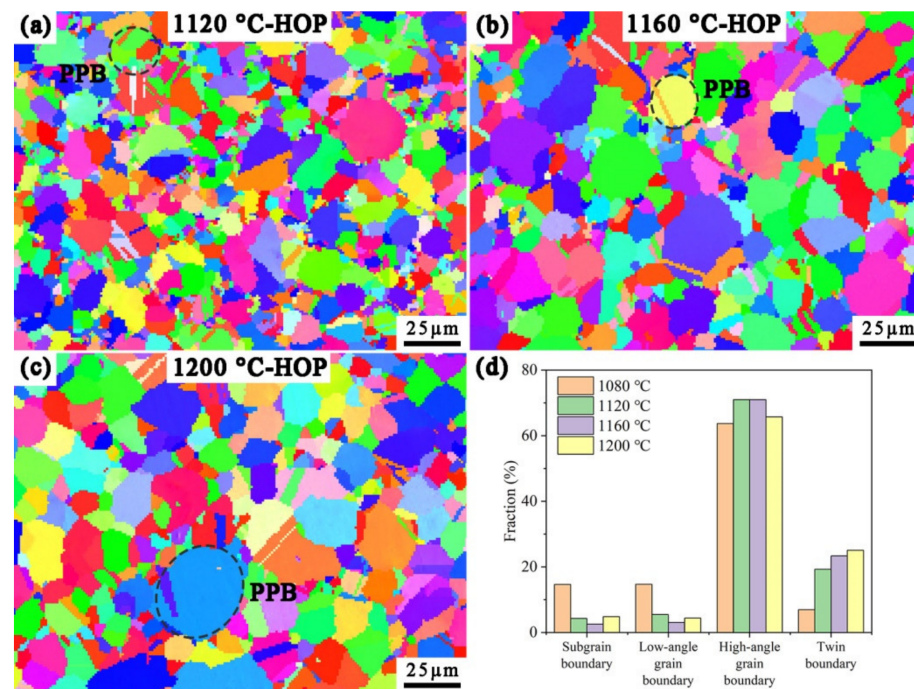


Figure 12. Inverse pole figure (IPF) of the samples: (a) 1080 °C-HOP; (b) 1120 °C-HOP; (c) 1160 °C-HOP; (d) 1200 °C-HOP; grain size distribution; (e) number fraction; (f) area fraction.

Table 2. The average grain size of the samples with various HOPing temperatures.

HOPing Temperature/°C	Grain Size (Number Fraction)/μm	Grain Size (Area Fraction)/μm
1080	6.08	9.09
1120	6.56	9.85
1160	8.58	14.28
1200	8.59	14.34

In addition, the microstructural feature, growth of twin crystals across the PPBs, is also observed in Figure 12b,d, with its local magnification being presented in Figure 13a,c. With the increasing HOPing temperature, the proportion of twin boundaries increases (Figure 13d). Many studies [18,33–35] also reported a similar microstructural feature and considered that cracks were prone to initiating and propagating near the PPBs precipitates, especially carbides and oxides. When some PPBs precipitates are trapped inside the grains, the paths for crack propagation are destroyed, thus improving the tensile properties of the materials.

**Figure 13.** Local magnification in Figure 12 of the samples: (a) 1120 °C-HOP; (b) 1160 °C-HOP; (c) 1200 °C-HOP and (d) grain boundary proportion.

On the other hand, with the increasing HOPing temperature, the PPBs scales gradually decrease (as shown in Figure 3). The quantity of PPBs precipitates is one of the important factors related to the PPBs scale. The relationship between the PPBs precipitates size and volume fraction is as follows:

$$V_i = Cd_i^3 \quad (1)$$

$$V = \sum_{i=1}^n V_i \quad (2)$$

where V_i is the volume fraction of the i th PPBs precipitates, d_i is the size of the i th PPBs precipitates, C is a constant related to its shape, and V is the sum of the volume fraction of all PPBs precipitates.

According to the results in Table 1 and Equation (1), the relationship between the size and the third square root of the volume fraction is plotted in Figure 14. With the increasing HOPing temperature, the size and volume fraction of precipitates increase, but

the curves become flat basically (slope decreased), which indicated that the number of PPBs precipitates decreased.

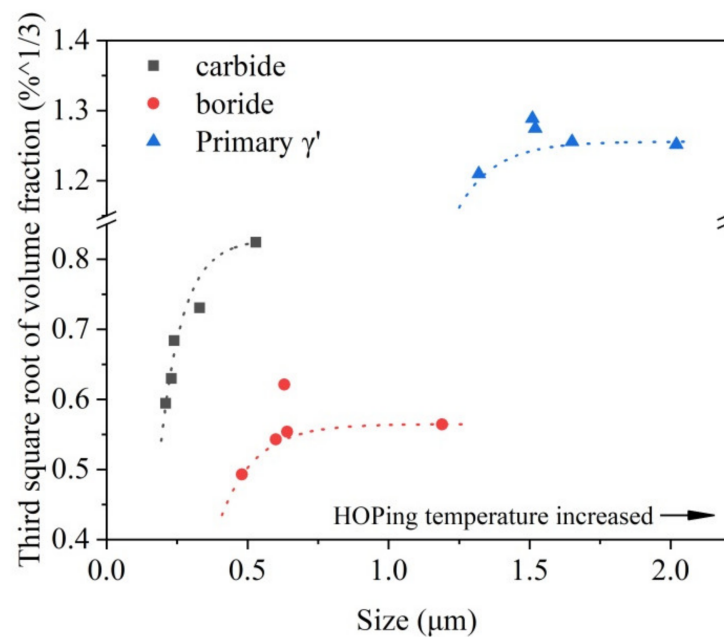


Figure 14. The relationship between size and volume fraction of PPBs precipitates.

The inhibition of PPBs is also related to the reduction of the size and volume fraction of borides and carbides with the increasing HOPing temperature (Figure 6e,f and Table 1). However, it is noted that in a specific range of temperatures, the volume fraction of PPBs precipitates does not rise with the increase in HOPing temperature, which mainly contains the following two aspects: (1). The volume fraction of boride in the 1200 °C-HOP sample is less than that in the 1160 °C-HOP sample; (2). The volume fraction of primary γ' phases decreases in the range of 1120–1200 °C.

For borides, the size increases with the increasing HOPing temperature. The study by Chang L. et al. [18] shows that the dissolution of γ' phases would provide boride-forming elements, leading to an increase in the borides. However, the volume fraction of borides in the 1200 °C-HOP sample is less than that in the 1160 °C-HOP sample. As the HOPing temperature increases to the boride solvus (1200 °C, as reported in [18]), some of the borides are dissolved, leading to the reduction of the boride volume fraction.

For the primary γ' phases, with the increasing HOPing temperature, its volume fraction increases at 1040–1080 °C and then decreases slightly. Some studies [36–38] show that the γ' solvus of FGH4096 is about 1120–1160 °C. DSC was carried out on the as-received powder, as shown in Figure 15. The γ' solvus is about 1135 °C, but the initial endothermic peak temperature is only 1068 °C. In the cooling process, the dissolution, nucleation, and growth of the γ' phases occur simultaneously, and the primary γ' , second γ' and tertiary γ' are precipitated successively. But the γ' phases are dominated by nucleation and growth when the HOPing temperature is less than 1068 °C, leading to an increase in their volume fraction and size. When the HOPing temperature reaches 1068 °C and above, the γ' phases are dissolved, and the volume fraction decreases. The volume fraction of γ' phases in the HOPed samples is listed in Table 3. The variation of the γ' phase volume fraction is consistent with the primary γ' phase. Some studies [39] show that the primary γ' phases could hinder grain boundary motion through the Zener pinning effect. Therefore, the grain size increases most from 1120 °C to 1160 °C due to the content of primary γ' phases decreases.

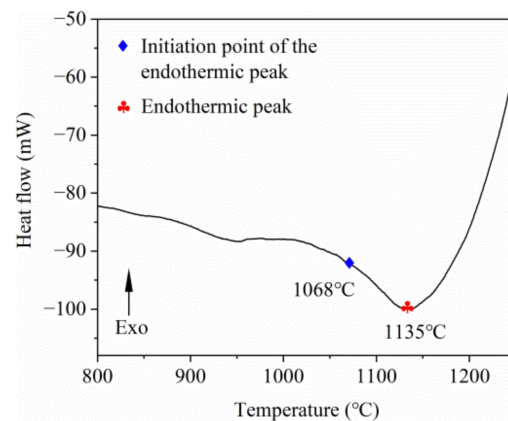


Figure 15. Heating DSC curve of FGH4096 powder.

Table 3. The volume fraction of γ' phases of the HOP samples.

HOPing Temperature/°C	The Volume Fraction of γ' /%
1040	38.52
1080	39.66
1120	38.22
1160	37.84
1200	35.75

4.2. Relationship between Microstructure and Tensile Property

The yield strength decreases with the increasing HOPing temperature (Figure 8). According to the Hall–Petch relationship, as follows:

$$\sigma_s = \sigma_0 + kd^{-1/2} \quad (3)$$

where σ_s is the yield strength, σ_0 is the lattice friction resistance when a single dislocation is moved, K is a constant related to the type of material, and d is the average grain size.

Due to the grain coarsening, the yield strength of the material decreases with the increasing HOPing temperature. But the increase of the sample grain size in the temperature range of 1120–1160 °C is more obvious than in other temperature ranges, while the decrease of the sample yield strength in the temperature range of 1120–1160 °C is almost the same as in other temperature ranges. The investigation of Cai C. et al. [40] shows that the increase in γ' phase volume fraction could compensate for the decrease in yield strength due to grain coarsening. It is seen that the decrease of γ' phase volume fraction at 1120–1160 °C is smaller than at other temperatures (as shown in Table 3), which offsets the decrease in yield strength due to grain growth. In addition, with the increasing HOPing temperature, the uniformity of grain size increases (Figure 13f), resulting in the more stable tensile properties of the material (Figure 8).

PPBs also have a significant effect on the tensile properties of the materials. With the increase in HOPing temperature, the PPBs scale decreases, but the tensile strength and elongation decrease significantly at the range of 1160–1200 °C. It can be attributed to the following two points:

1. The coarsened PPBs precipitates lead to a decrease in fracture toughness at the interface between the PPBs precipitates and the γ matrix, and the cracks are more likely to initiate and propagate at this interface. The research results of Zhang Y. et al. [41] show that precipitations on particle boundaries hinder dislocation movement and lead to dislocation pileup. The larger the precipitate size is, the more likely it is to produce the stress concentration at the precipitates and lead to accelerating crack propagation in the area of weak fracture toughness, presenting inter-particle fracture in the sample. The PPBs precipitate size in the 1200 °C-HOP is significantly larger

than that in the 1160 °C-HOP, thus the severe stress concentration and dislocation pileup lead to a decrease in the plasticity of the 1200 °C-HOP sample (Figure 8).

2. The intensive dispersion of borides at PPBs is also the reason for the reduction of the tensile properties of materials. As a grain boundary strengthening element, B is added to superalloy powder. But according to the study of Witt M. et al. [42], when the materials HIPed at a high temperature, the B element was more likely to segregate at PPBs and form large borides. It is also presented in this work, as shown in Figure 6. The borides in the 1160 °C-HOP sample are small in size and mainly distributed inside the particles, while the borides in the 1200 °C-HOP sample are large and mainly distributed at PPBs. On the one hand, the intensive dispersion of borides at PPBs leads to the strengthening effect of B on grain boundaries being weakened, which significantly decreases the strength and plasticity of the material, presenting the intergranular fracture in the material. On the other hand, the large borides are more prone to initiating cracks. The segregation of borides at PPBs promotes the initiation and propagation of microcracks, which damages the tensile properties of the material.

4.3. The Effect of Oscillatory Pressure on Microstructure and Tensile Properties

It is seen that the tensile properties of the 1200 °C-HOP sample are significantly higher than those of 1200 °C-HP sample. It can be attributed to the following two reasons:

1. The PPBs scale is higher in the 1200 °C-HP (Figure 3). The size and volume fraction of the borides and carbides in the 1200 °C-HP are larger than those in the 1200 °C-HOP. The size and volume fraction of the primary γ' phases are similar in these two samples. More PPBs precipitates damage the tensile properties of the 1200 °C-HP sample;
2. More borides aggregate at PPBs in the 1200 °C-HP sample (Figure 6). Compared with the 1200 °C-HOP sample, the B elements segregate at PPBs, leading to the grain boundary strengthening being weakened, and microcracks are more prone to initiating and propagating near the borides (Figure 11).

Based on the results, compared with HP, it has some positive effects on microstructure, especially the inhibition of PPBs. HOP has been shown to promote powder sliding and deformation [26–31]. And some studies [17,43] show that pre-heating of powder could inhibit PPBs. HOP plays a similar role to powder preheating treatment. However, compared with additional preheating, HOP is more economical.

5. Conclusions

The microstructure and tensile properties of the samples with various processes were analyzed, and the following conclusions can be drawn:

1. Stress concentration is prone to be generated at the pores, which provides the path for crack initiation and propagation. It is the reason that poor tensile properties are presented in the samples HOPed at a low temperature (1040 °C-HOP);
2. With the increase in HOPing temperature, grain coarsens, the PPBs scale decreases and the PPBs precipitates change from primary γ' phases dominated to mainly borides and carbides, thus the yield strength decreases and the ultimate tensile strength and elongation increase first and then decrease;
3. The highest ultimate tensile strength and elongation of 1403 MPa and 35 %, respectively, are reached when the HOPing temperature is 1160 °C;
4. Compared with the HP process, the HOP could decrease the size and density of the PPBs precipitates and significantly enhance their room temperature tensile properties.

Author Contributions: Methodology, G.L. and D.S.; validation, G.L.; investigation, J.K., data curation, J.K. and Y.G.; writing—original draft preparation, G.L.; writing—review and editing, D.S.; project administration, Y.G. and Q.G.; supervision, Q.G., X.Y. and K.G.; conceptualization, X.Y. All authors have read and agreed to the published version of the manuscript.

Funding: This research was funded by National Natural Science Foundation of China (51904276, 51904277), Science and Technology Development Program of Henan Province (202102210013), Aviation Science Foundation of China (2018ZF55015).

Institutional Review Board Statement: Not applicable.

Informed Consent Statement: Not applicable.

Data Availability Statement: Not applicable.

Acknowledgments: The Beijing CISRI-GAONA Materials & Technology Co. Ltd. is thanked for providing the FGH4096 powders used in this work. The authors acknowledge the support of the Henan Provincial Key Laboratory of Aeronautical Materials and Application Technology.

Conflicts of Interest: The authors declare no conflict of interest.

References

1. Gloria, A.; Montanari, R.; Richetta, M.; Varone, A. Alloys for Aeronautic Applications: State of the Art and Perspectives. *Metals* **2019**, *9*, 662. [[CrossRef](#)]
2. Fecht, H.; Furrer, D. Processing of Nickel-Base Superalloys for Turbine Engine Disc Applications. *Adv. Eng. Mater.* **2000**, *2*, 777–787. [[CrossRef](#)]
3. Zhu, G.; Li, S.; Wang, R.; Wang, D.; Dong, A.; Shu, D.; Zhang, L.; Sun, B. In-situ SEM investigation on fracture behavior of GTD222 superalloy during tensile process at 760 °C. *J. Mater. Res.* **2020**, *9*, 15185–15190. [[CrossRef](#)]
4. Guo, X.; Zheng, W.; An, W.; Antonov, S.; Li, L.; Cormier, J.; Feng, Q. High temperature creep behavior of a cast polycrystalline nickel-based superalloy K465 under thermal cycling conditions. *Materialia* **2020**, *14*, 100913. [[CrossRef](#)]
5. Shang, Z.; Niu, H.; Wei, X.; Song, D.; Zou, J.; Liu, G.; Liang, S.; Nie, L.; Gong, X. Microstructure and tensile behavior of nickel-based single crystal superalloys with different Re contents. *J. Mater. Res. Technol.* **2022**, *12*, 2458–2469. [[CrossRef](#)]
6. Orozco-Caballero, A.; Gutierrez, C.; Gan, B.; Jon, M.M. High-throughput nanoindentation mapping of cast IN718 nickel-based superalloys: Influence of the Nb concentration. *J. Mater. Res.* **2021**, *36*, 2213–2222. [[CrossRef](#)]
7. Zhang, F.; Wang, C.; Wu, Y.; Zhou, L.; Tian, Q. Microstructural stability and mechanical properties of GH742 Ni-based wrought superalloy for turbine disk applications. *Mater. Sci. Eng. A* **2022**, *832*, 142488. [[CrossRef](#)]
8. Kumar Godasu, A.; Prakash, U.; Mula, S. Flow stress characteristics and microstructural evolution of cast superalloy 625 during hot deformation. *J. Alloys Compd.* **2020**, *844*, 156200. [[CrossRef](#)]
9. Sahithya, K.; Balasundar IPant, P.; Raghu, T. Comparative study on the high temperature deformation behaviour of an as-cast Ni base superalloy subjected to different cooling rates after homogenization. *J. Alloys Compd.* **2020**, *849*, 156626. [[CrossRef](#)]
10. Hu, B.; Liu, G.; Jia, C.; Tian, G. Development in new type high performance P/M superalloys. *J. Mater. Eng.* **2007**, *2*, 49–53.
11. Zhang, G.; Zhang, Y.; Zheng, L.; Peng, Z. Research Progress in Powder Metallurgy Superalloys and Manufacturing Technologies for Aero-Engine Application. *Acta Metall. Sin.* **2019**, *55*, 1133–1144.
12. Helle, A.; Easterling, K.; Ashby, M. Hot-isostatic pressing diagrams: New developments. *Acta Metall.* **1985**, *33*, 2163–2174. [[CrossRef](#)]
13. Qin, Z.; Liu, C.; Wang, Z.; He, G.; Liu, F.; Huang, L.; Jiang, L. Formation and microstructure evolution of precipitation on prior particle boundaries in P/M nickel-base superalloys. *Chin. J. Nonferrous Met.* **2016**, *1*, 50–59. [[CrossRef](#)]
14. Zhou, J.; Liu, C.; Zhao, W.; Zheng, Z.; Zhong, Y. Prior Particle Boundary of PM FGH96 Superalloy and Its In-situ High-cycle Fatigue at Elevated Temperature. *J. Aeronaut. Mater.* **2017**, *37*, 83–89. [[CrossRef](#)]
15. Lee, J.; Kim, Y.; Seo, S.; Lee, K. Effects of hot isostatic pressing treatment on the microstructure and tensile properties of Ni-based superalloy CM247LC manufactured by selective laser melting. *Mater. Sci. Eng. A* **2022**, *841*, 143083. [[CrossRef](#)]
16. Liu, M.; Zhang, Y.; Liu, P.; Zhang, Y. Study on the PPB defect of P/M superalloy FGH95. *Powder Metall. Ind.* **2006**, *3*, 1–5. [[CrossRef](#)]
17. Qiu, C.L.; Attallah, M.M.; Wu, X.H.; Andrews, P. Influence of hot isostatic pressing temperature on microstructure and tensile properties of a nickel-based superalloy powder. *Mater. Sci. Eng. A* **2013**, *564*, 176–185. [[CrossRef](#)]
18. Chang, L.; Sun, W.; Cai, Y.; Yang, R. Microstructure, Tensile Properties, and Hot-Working Characteristics of a Hot Isostatic-Pressed Powder Metallurgy Superalloy. *Metall. Mater. Trans. A* **2017**, *48*, 1273–1287. [[CrossRef](#)]
19. Bai, Q.; Lin, J.; Tian, G.; Zou, J.; Dean, T. Review and Analysis of Powder Prior Boundary (PPB) Formation in Powder Metallurgy Processes for Nickel-based Super Alloys. *J. Powder Metall. Min.* **2015**, *4*, 1000127.
20. Ning, Y.; Yao, Z.; Li, H.; Guo, H.; Tao, Y.; Zhang, Y. High temperature deformation behavior of hot isostatically pressed P/M FGH4096 superalloy. *Mater. Sci. Eng. A* **2010**, *527*, 961–966. [[CrossRef](#)]
21. Wen, H.; Tang, X.; Jin, J.; Cai, C.; Yang, H.; Teng, Q.; Wei, Q.; Wang, X.; Zheng, C.; He, Y.; et al. Effect of extrusion ratios on microstructure evolution and strengthening mechanisms of a novel P/M nickel-based superalloy. *Mater. Sci. Eng. A* **2022**, *847*, 143356. [[CrossRef](#)]
22. Lizzi, F.; Pradeep, K.; Stanojevic, A.; Sommadossi, S.; Poletti, M.C. Hot Deformation Behavior of a Ni-Based Superalloy with Suppressed Precipitation. *Metals* **2021**, *11*, 605. [[CrossRef](#)]

23. Rao, G.; Srinivas, M.; Sarma, D. Effect of thermomechanical working on the microstructure and mechanical properties of hot isostatically pressed superalloy Inconel 718. *Mater. Sci. Eng. A* **2004**, *383*, 201–212. [[CrossRef](#)]
24. Tan, G.; Li, H.; Wang, Y.; Yang, L.; Qiao, S.; Huang, Z.; Liu, M. Hot working characteristics of HEXed PM nickel-based superalloy during hot compression. *Trans. Nonferrous Metal. Soc. China* **2020**, *30*, 2709–2723. [[CrossRef](#)]
25. Xie, Z.; Li, S.; An, L. A novel oscillatory pressure-assisted hot pressing for preparation of high performance ceramics. *J. Am. Ceram. Soc.* **2014**, *97*, 1012–1015. [[CrossRef](#)]
26. Yuan, Y.; Fan, J.; Li, J.; Liu, J.; Zhao, K.; Liu, D.; An, L. Oscillatory pressure sintering of Al₂O₃ ceramics. *Ceram. Int.* **2020**, *46*, 15670–15673. [[CrossRef](#)]
27. Gao, K.; Xu, Y.; Tang, G.; Fan, L.; Zhang, R.; An, L. Oscillating pressure sintering of W–Ni–Fe refractory alloy. *J. Alloys Compd.* **2019**, *805*, 789–793. [[CrossRef](#)]
28. Gao, Y.; Gao, K.; Fan, L.; Yang, F.; Guo, X.; Zhang, R.; An, L. Oscillatory pressure sintering of WC-Fe-Ni cemented carbides. *Ceram. Int.* **2020**, *46*, 12727–12731. [[CrossRef](#)]
29. Fan, J.; Yuan, Y.; Li, J.; Liu, J.; Zhao, K.; Liu, D.; An, L. Densification and grain growth in oscillatory pressure sintering of alumina toughened zirconia ceramic composites. *J. Alloys Compd.* **2020**, *845*, 155644. [[CrossRef](#)]
30. Liu, D.; Zhang, X.; Fan, J.; Yuan, Y.; Zhao, K.; Liu, J.; An, L. Sintering behavior and mechanical properties of alumina ceramics exposed to oscillatory pressure at different sintering stages. *Ceram. Int.* **2021**, *47*, 23682–23685. [[CrossRef](#)]
31. Sun, D.; Zhao, K.; Li, G.; Kang, J.; Gao, K.; Zhang, Z.; Gao, Y.; Fan, L.; An, L. Hot oscillating pressed FGH4096 nickel-based alloy with enhanced ductility and strength. *J. Alloys Compd.* **2022**, *894*, 162366. [[CrossRef](#)]
32. Ingesten, N.; Warren, R.; Winberg, L. *The Nature and Origin of Previous Particle Boundary Precipitates in P/M Superalloys*; Springer: Dordrecht, The Netherlands, 1982; pp. 1013–1027.
33. Tan, L.; He, G.; Liu, F.; Li, Y.; Jiang, L. Effects of Temperature and Pressure of Hot Isostatic Pressing on the Grain Structure of Powder Metallurgy Superalloy. *Materials* **2018**, *11*, 328. [[CrossRef](#)] [[PubMed](#)]
34. Sreenu, B.; Sarkar, R.; Satheesh Kumar, S.S.; Chatterjee, S.; Appa Rao, G. Microstructure and mechanical behaviour of an advanced powder metallurgy nickel base superalloy processed through hot isostatic pressing route for aerospace applications. *Mater. Sci. Eng. A* **2020**, *797*, 140254. [[CrossRef](#)]
35. Chang, L.; Sun, W.; Cui, Y.; Yang, R. Influences of hot-isostatic-pressing temperature on microstructure, tensile properties and tensile fracture mode of Inconel 718 powder compact. *Mater. Sci. Eng. A* **2014**, *599*, 186–195. [[CrossRef](#)]
36. Fang, B.; Ji, Z.; Tian, G.; Jia, C. Investigation on complete solution temperature of γ' in the P /M superalloy of FGH96. *Powder Metal. Technol.* **2013**, *31*, 89–95. [[CrossRef](#)]
37. Li, C.; Chen, L.; Qu, Z.; Lai, Y.; Liang, S. Measurement of complete dissolution temperature of γ' phase in nickel-based P /M superalloy FGH4096. *Heat Treat. Met.* **2021**, *46*, 174–177. [[CrossRef](#)]
38. Qiu, C.; Yang, D.; Wang, G.; Liu, Q. Microstructural development and tensile behavior of a hot isostatically pressed nickel-based superalloy. *Mater. Sci. Eng. A* **2020**, *769*, 138461. [[CrossRef](#)]
39. Alvarado, K.; Janeiro, I.; Florez, S.; Flipon, B.; Franchet, J.-M.; Locq, D.; Dumont, C.; Bozzolo, N.; Bernacki, M. Dissolution of the Primary γ' Precipitates and Grain Growth during Solution Treatment of Three Nickel Base Superalloys. *Metals* **2021**, *11*, 1921. [[CrossRef](#)]
40. Cai, C.; Pan, K.; Teng, Q.; Gao, X.; Song, B.; Liu, J.; Wei, Q.; Zhou, K.; Shi, Y. Simultaneously enhanced strength and ductility of FGH4097 nickel-based alloy via a novel hot isostatic pressing strategy. *Mater. Sci. Eng. A* **2019**, *760*, 19–25. [[CrossRef](#)]
41. Zhang, Y.; Zhang, Y.; Sun, Z.; Huang, H. Influence of PPB on Crack Growth Behavior of PM Ni-Based Superalloy. *Rare Metal Mat. Eng.* **2019**, *48*, 3282–3288.
42. Witt, M.; Charles, J. Boride particles in a powder metallurgy superalloy. *Mater. Sci. Technol.* **1985**, *1*, 1063–1068. [[CrossRef](#)]
43. Liu, J.; Zhang, Y. AES analysis and pre-heat treatment of FGH96 superalloy powders. *Chin. J. Nonferrous Met.* **2012**, *22*, 2797–2803.